Received 13 February 2022; | Revised ; | Accepted: 00 Month 0000

DOI: xxx/xxxx

RESEARCH ARTICLE

Deconvolution closure for mesoscopic continuum models of particle systems

Alexander Panchenko*[1] | Lyudmyla L. Barannyk[2] | Kevin Cooper[1]

[1]Department of Mathematics, Washington State University, WA, USA
[2]Department of Mathematics and Statistical Science, University of Idaho, ID, USA

Correspondence
*Corresponding author, Email: panchenko@math.wsu.edu

Summary

We present a framework for derivation of closed-form continuum equations governing mesoscale dynamics of large particle systems. Balance equations for spatial averages such as density, linear momentum, and energy were previously derived by a number of authors. These equations are exact, but are not in closed form because the stress and the heat flux (e.g. stress in the momentum balance equation) cannot be evaluated without the knowledge of particle positions and velocities. Recently, we proposed a method for approximating exact fluxes by true constitutive equations, that is, using non-local operators acting only on the average density and velocity. In the paper, constitute operators are obtained by using filtered regularization methods from the theory of ill-posed problems. We also formulate conditions on fluctuation statistics which permit approximating these operators by local equations. The performance of the method is tested numerically using Fermi-Pasta-Ulam particle chains with two different potentials: the classical Lennard-Jones, and the purely repulsive potential used in granular materials modeling. The initial conditions incorporate velocity fluctuations on scales that are smaller than the size of the averaging window. Simulation results show good agreement between the exact stress and its closed form approximation.

KEYWORDS:
FPU chain, particle chain, oscillator chain, upscaling, model reduction, dimension reduction, closure

1 | INTRODUCTION

Particle systems governed by Newton's ordinary differential equations (ODEs) are common in physics, engineering and computational biology. Such systems could represent either classical atomistic models, or discretizations of continuum mechanical partial differential equations (PDEs). In particular, ODE models have long been used in modeling solid state (see, e.g., [1,2,3,4]).

Often, the ODE solutions are of secondary interest compared with various space-time averages. Examples of the latter are density, velocity, stress, deformation gradient, and energy. The averages can always be simulated directly, but this may be of limited usefulness owing to the large size and stiffness of the underlying ODEs. Popular explicit solvers such as Verlet method require small time steps, which places severe restrictions on the length of the simulated time interval. When direct simulation is infeasible, an averaging procedure can be used to derive continuum style equations.

The theory of averaging for particle systems was developed by several authors, starting with Irving and Kirkwood[5] and Noll[6] who emphasized ensemble averages. Space and time averaging was developed by Hardy[7] and Murdoch and Bedeaux[8,9,10,11].

Noll ensemble averaging was extended to rod-like particles in [12,13]. Extension to multi-body potentials was developed in [14]. An interesting version of the averaging procedure based on Galilean invariance is proposed in [15].

The averaging in these works is done as follows. First, one selects the *primary averages* that would describe the system at the mesoscale. These may be, for example, average density, velocity, deformation map, kinetic energy etc. Next, differentiating in time and using the ODEs, one obtains exact balance equations for the primary averages. The fluxes (or *secondary averages*) in these equations are given by explicit functionals of the ODE solutions.

While important for clarifying the relationship between micro- and mesoscale phenomena, results of this type do not provide a continuum model in the true sense of the word, because one still has to solve the ODEs to evaluate the fluxes. Therefore, the balance equations in [8] are not in closed form. In classical continuum mechanics, constitutive equations express stress and heat flux in terms of velocity gradient, deformation gradient, and temperature. In the above referenced theories, the average deformation and temperature are not sufficient for evaluating fluxes, because one still has to recover the positions and velocities of all particles. As a result, the complexity of the mesoscale models in [8] and [7] is about the same as the complexity of the ODE model.

In this paper, we present a method for approximating fluxes in terms of the primary averages. The approximations have the same low complexity as classical constitutive equations, but unlike these equations, our approximations combine explicit formulas and numerical algorithmic prescriptions. From our point of view, any constitutive equation will be ultimately realized as a computational scheme. The accuracy and efficiency of this scheme are the main factors that determine the quality of the theory. Therefore, instead of postulating simple constitutive equations with experimentally fitted material parameters, we aim to develop a systematic computational approach satisfying three criteria: (i) it does not require solving the ODE system; (ii) it clearly and consistently incorporates the known micro-scale information such as force equations and initial conditions; and (iii) it permits accurate reproduction of exact fluxes.

To explain the main idea, suppose that the primary averages are spatially averaged density and velocity. These averages can be approximated by convolutions of the given “window function" with certain *recoverable* functions of particle velocities and positions. In this way, each primary average is related to one recoverable function. Convolution can be approximately inverted. This results in *deconvolution approximations* of recoverable functions by operators acting on primary averages. Next, the exact stress is written as a non-linear integral operator acting on the recoverable functions. Replacing the exact recoverable functions with their deconvolution approximations yields a true constitutive equation. The stress in this equation is now an operator acting on the density and velocity.

Deconvolution problem is unstable (ill-posed) so that small perturbations of the averages can produce large perturbations in the recovered functions. Ill-posed problems are well studied in the literature (see e.g. [16,17,18,19,20]) in both continuous and discrete settings. A discrete version of the convolution integral equation is an ill-conditioned linear system. Such systems and related rank-deficient systems are treated in detail in the book [21].

The stress in the resulting constitutive equations depends on density and momentum in a non-local and non-linear manner. This is similar to the peri-dynamical formulation of continuum mechanics [22]. The difference between our approach and phenomenological peri-dynamics is that we provide a link between the microscale features of the particle dynamics and mesoscale constitutive equations. On the other hand, this work differs from the recent paper [23] where the peri-dynamic stress and energy flux are given as exact functions of particle positions and velocities. The theory developed here allows evaluation of the stress without solving the ODE system.

We tested the method numerically on one-dimensional systems interacting with either Lennard-Jones potential or a purely repulsive potential reminiscent of the Hertz potential of granular acoustics. The Lennard-Jones potential was chosen because of its usefulness for modeling amorphous solids and liquid-solid phase transitions [24,25,26,27].

Assuming that the mesoscale state of a system is isothermal and thus can be described by the density and linear momentum, we provide the corresponding balance equations and derive constitutive equations for the stress. The exact stress and exact primary averages are produced by the direct simulations with 10,000 particles. The approximate stresses are obtained by using deconvolution and then substituting into the formulas for the exact stress. Then we compare the exact and approximate stresses rendered on the mesoscale mesh with 500 nodes. The results show that the approximation agrees very well with the exact stress.

In the earlier works [28], [29] we used a simpler version of the proposed method to deal with the formal finite-difference discretizations of hyperbolic PDEs ([28]), and discrete models of fluids ([29]). In both papers, the suggested deconvolution algorithm was the classical Landweber iteration [30], [31]. Increasing the number of iterations n increases accuracy but generally decreases stability. The zero-order approximation ($n = 0$) consists of replacing microscale quantities with their averages. This zero-order closure, similar to the quasi-continuum method [32], [33], was the only situation considered in [28] in detail. In [29] we also used the first- and

second-order approximations. Numerical experiments show that these low-order closures work well when the initial velocity has small fluctuations, and the dynamics is nearly isothermal, meaning that the energy of velocity fluctuations is much smaller than the potential energy.

The present article extends and improves the method introduced in [28]. We derive new multidimensional closed form approximations for the stress and conduct numerical experiments designed to test the performance of the method for non-equilibrium particle systems with non-convex potentials such as Lennard-Jones. Unlike [28], where we employed non-oscillatory initial conditions, here we work with the initial conditions that contain prominent small scale features, oscillations, and noise. The Landweber iteration is simple and useful for modeling, but has a slow convergence rate (see [21]). For initial conditions with high fluctuations, a large number of iterations may be needed to achieve a reasonable accuracy. In this work we use different techniques: regularization by discretization [17] and truncated singular value decomposition (SVD) (see, e.g. [21]). Both methods are non-iterative. Regularization by discretization is straightforward: the integral is approximated by a numerical quadrature, and this eliminates accumulation of the spectrum to zero. In the truncated SVD method, the exact solution is represented in the basis of singular vectors. The regularized approximation is generated by discarding the components corresponding to the smallest singular values. Using SVD yields additional computational savings, since the convolution kernel is dynamics-independent. The SVD of the kernel can be pre-computed and used repeatedly with different ODE systems. In the recent paper [34], we analyzed numerically performance of the deconvolution closure technique based on the truncated SVD method depending on the choice of the averaging window function, the value of the mesoscale resolution parameter, scale separation, the level of filtering of singular values and the level of spectral filtering of the averages. We also provided partial error estimates for filtered regularization methods.

Recently, a deconvolution approach was used in large eddy simulation (LES) of turbulence [35], [36], [37], [38]. In these works, deconvolution was used to approximate quadratic functions of velocity fluctuations by an operator acting on the average velocity. The present work differs from LES in two respects. The first difference is in the structure of the averaging operators. In LES, the average velocity depends linearly on the microscale velocity, while in our work this dependence is non-linear. This non-linearity makes it possible to handle the general ODE flows with non-constant Jacobians. The second difference is in the modeling. We provide the connection between Newtonian particle mechanics on the one hand, and continuum theories on the other hand. In LES, the objective is to simulate large scale features of flows governed by Navier-Stokes equations.

The paper is organized as follows. In Section 2 we describe a general multi-dimensional microscopic model and provide the exact balance equations for the averages, following [8], [11]. In Section 3 we develop general multi-dimensional integral approximations of averages, and describe the use of regularization for approximate deconvolution. This is the central section of the paper. In Section 4 we derive closed form balance equations of mass and momentum for FPU chains. In practice it is often useful to have local constitutive equations. Such equations are given by ordinary functions instead of integral operators. In the present framework, local equations can be obtained under certain conditions on the ODE dynamics. These conditions and the resulting constitutive equations are derived in Section 5. Section 6 contains the results of computational tests. Finally, conclusions are given in Section 7.

2 | MICROSCALE EQUATIONS AND MESOSCALE SPATIAL AVERAGES

2.1 | Scaled ODE problems

We work with classical Newton equations of point particle dynamics. The same equations arise as discretization of the momentum balance equation for continuum systems. Consider a system containing $N \gg 1$ identical particles, denoted by P_i. The mass of each particle is $\frac{M}{N}$, where M is the total mass of the system. Suppose that during the observation time T, P_i remain inside a bounded domain Ω in $\mathbb{R}^d$, where d is the physical space dimension, usually $1, 2$ or 3. The positions $\boldsymbol{q}_i(t)$ and velocities $\boldsymbol{v}_i(t)$ of particles satisfy a system of ODEs

$$\dot{\boldsymbol{q}}_i = \boldsymbol{v}_i, \tag{2.1}$$

$$\frac{M}{N}\dot{\boldsymbol{v}}_i = \boldsymbol{f}_i + \boldsymbol{f}_i^{(ext)}, \tag{2.2}$$

subject to the initial conditions

$$\boldsymbol{q}_i(0) = \boldsymbol{x}_i, \qquad \boldsymbol{v}_i(0) = \boldsymbol{v}_i^0. \tag{2.3}$$

Here $\boldsymbol{f}_i^{(ext)}$ denotes external forces, such as gravity and confining forces. The interparticle forces $\boldsymbol{f}_i = \sum_j \boldsymbol{f}_{ij}$, where $\boldsymbol{f}_{ij}$ are pair interaction forces generated by a finite range potential U. The forces are scaled by a microscale distance parameter ε

$$\varepsilon = N^{-1/d}. \tag{2.4}$$

The purpose of the scaling is to satisfy the following natural requirements. As $N \to \infty$, the total mass of the system should remain fixed, and the total particle potential energy should be either fixed, or at least bounded independent of N. Accordingly we set

$$\boldsymbol{f}_{ij} = -\frac{1}{N}\nabla_{\boldsymbol{q}_i} U\left(\frac{|\boldsymbol{q}_i - \boldsymbol{q}_j|}{\varepsilon}\right) = -\frac{1}{\varepsilon N}\frac{d}{d\xi}U(\xi)\Big|_{\xi=|\boldsymbol{q}_i-\boldsymbol{q}_j|}\frac{\boldsymbol{q}_i - \boldsymbol{q}_j}{|\boldsymbol{q}_i - \boldsymbol{q}_j|}. \tag{2.5}$$

2.2 | Length scales

A parameter $\eta > 0$ characterizes spatial mesoscale resolution. This parameter can be chosen based on the desired accuracy, computational cost requirements, and prior information about initial conditions and ODE trajectories. Depending on the relationship between η and ε, different situations may be of interest. Here we consider only the *mesoscale regime*, for which $\eta \gg \varepsilon$, and η is fixed as $\varepsilon \to 0$ (equivalently $N \to \infty$).

2.3 | Averages and their evolution

The mesoscopic average density and momentum are given, respectively, by ([7],[8])

$$\overline{\rho}^{\eta}(t, \boldsymbol{x}) = \frac{M}{N}\sum_{i=1}^{N} \psi_{\eta}(\boldsymbol{x} - \boldsymbol{q}_i(t)), \tag{2.6}$$

$$\overline{\rho}^{\eta}\overline{\boldsymbol{v}}^{\eta}(t, \boldsymbol{x}) = \frac{M}{N}\sum \boldsymbol{v}_i(t)\psi_{\eta}(\boldsymbol{x} - \boldsymbol{q}_i(t)), \tag{2.7}$$

where the scale-dependent window function ψ_{η} is defined by

$$\psi_{\eta}(\boldsymbol{x}) = \eta^{-d}\psi\left(\frac{\boldsymbol{x}}{\eta}\right) \tag{2.8}$$

starting from a fixed differentiable function ψ satisfying $\int \psi \, d\boldsymbol{x} = 1$.

Differentiating (2.6), (2.7) in t, and using the ODEs (2.1), (2.2) one can obtain[7,8] exact balance equations for the primary variables. For an isolated system with ($\boldsymbol{f}_i^{(ext)} = 0$), mass conservation and momentum balance equations take the form:

$$\partial_t \overline{\rho}^{\eta} + \operatorname{div}(\overline{\rho}^{\eta}\overline{\boldsymbol{v}}^{\eta}) = 0, \tag{2.9}$$

$$\partial_t(\overline{\rho}^{\eta}\overline{\boldsymbol{v}}^{\eta}) + \operatorname{div}\left(\overline{\rho}^{\eta}\overline{\boldsymbol{v}}^{\eta} \otimes \overline{\boldsymbol{v}}^{\eta}\right) - \operatorname{div}\boldsymbol{T}^{\eta} = 0. \tag{2.10}$$

The stress $\boldsymbol{T}^{\eta} = \boldsymbol{T}^{\eta}_{(c)} + \boldsymbol{T}^{\eta}_{(int)}$[11], where

$$\boldsymbol{T}^{\eta}_{(c)}(t, \boldsymbol{x}) = -\sum m_i(\boldsymbol{v}_i - \overline{\boldsymbol{v}}^{\eta}(t, \boldsymbol{x},)) \otimes (\boldsymbol{v}_i - \overline{\boldsymbol{v}}^{\eta}(\boldsymbol{x}, t))\psi_{\eta}(\boldsymbol{x} - \boldsymbol{q}_i) \tag{2.11}$$

is the *convective stress*, and

$$\boldsymbol{T}^{\eta}(t, \boldsymbol{x})_{(int)} = \sum_{(i,j)} \boldsymbol{f}_{ij} \otimes (\boldsymbol{q}_j - \boldsymbol{q}_i)\int_0^1 \psi_{\eta}\left(s(\boldsymbol{x} - \boldsymbol{q}_j) + (1-s)(\boldsymbol{x} - \boldsymbol{q}_i)\right) ds \tag{2.12}$$

is the *interaction stress*. The summation in (2.12) is over all pairs of particles (i, j) that interact with each other.

Equations (2.9), (2.10) are written in the spatial (Eulerian) frame. For material science applications, it may be more convenient to use the referential (Lagrangian) formulation. Upon defining the mesoscale deformation map $\boldsymbol{\psi}^{\eta}(t, \boldsymbol{X})$ satisfying

$$\partial_t \boldsymbol{\psi}^{\eta}(t, \boldsymbol{X}) = \overline{\boldsymbol{v}}^{\eta}(t, \boldsymbol{\psi}^{\eta}(t, \boldsymbol{X})), \qquad \boldsymbol{\psi}(0, \boldsymbol{X}) = \boldsymbol{X}, \tag{2.13}$$

one can derive in the usual manner the mass conservation

$$\overline{\rho}^{\eta}(t, \boldsymbol{\psi}(t, \boldsymbol{X})) = \overline{\rho}^{\eta}_0(\boldsymbol{X}),$$

where $\overline{\rho}_0^\eta$ is the initial density. The momentum conservation takes the form

$$\overline{\rho}_0^\eta \partial_{tt} \boldsymbol{\psi}^\eta = \text{Div } \boldsymbol{P}^\eta, \tag{2.14}$$

where Div denotes the divergence with respect to $\boldsymbol{X}$,

$$\boldsymbol{P}^\eta = (\det \boldsymbol{F}^\eta)\, \boldsymbol{T}^\eta(t, \boldsymbol{\psi}^\eta(t, \boldsymbol{X}))\left(\boldsymbol{F}^{-1,\eta}\right)^T$$

is the first Piola-Kirchhoff stress tensor, and $\boldsymbol{F}^\eta(t, \boldsymbol{X}) = \nabla_{\boldsymbol{X}} \boldsymbol{\psi}^\eta(t, \boldsymbol{X})$ is the deformation gradient.

3 | CLOSURE VIA REGULARIZED DECONVOLUTIONS

3.1 | Outline

Our approach is based on a simple idea: the integral approximations of primary averages (such as density and velocity) are related to the corresponding microscopic quantities via convolution with the kernel ψ_η. Therefore, given primary variables we can (approximately) recover the microscopic positions and velocities by numerically inverting convolution operators. The results are inserted into equations for secondary averages (or fluxes), such as stress in the momentum balance. This yields closed form balance equations that can be simulated efficiently on the mesoscopic mesh.

3.2 | Integral approximation of discrete averages

3.2.1 | Primary averages

The special structure of the average momentum and density is revealed by approximating the sums in (2.6) and (2.7) by integrals ([28]):

$$\overline{\rho}^\eta(t, \boldsymbol{x}) = \frac{M}{N} \sum_{i=1}^N \psi_\eta(\boldsymbol{x} - \boldsymbol{q}_i(t)) = \frac{M}{|\Omega|} \int\limits_\Omega \psi_\eta(\boldsymbol{x} - \tilde{\boldsymbol{q}}(t, \boldsymbol{X}))d\boldsymbol{X} = \frac{M}{|\Omega|} \int\limits_\Omega \psi_\eta(\boldsymbol{x} - \boldsymbol{y})J(t, \boldsymbol{y})d\boldsymbol{y}, \tag{3.1}$$

$$\overline{\rho}^\eta \overline{\boldsymbol{v}}^\eta(t, \boldsymbol{x}) = \frac{M}{|\Omega|} \int\limits_\Omega \tilde{\boldsymbol{v}}(t, \tilde{\boldsymbol{q}}(t, \boldsymbol{X}))\psi_\eta(\boldsymbol{x} - \tilde{\boldsymbol{q}}(t, \boldsymbol{X}))d\boldsymbol{X} = \frac{M}{|\Omega|} \int\limits_\Omega \psi_\eta(\boldsymbol{x} - \boldsymbol{y})\tilde{\boldsymbol{v}}(t, \boldsymbol{y})J(t, \boldsymbol{y})d\boldsymbol{y}. \tag{3.2}$$

Equality in (3.1), (3.2) holds up to a discretization error. The function $\tilde{\boldsymbol{q}}$ is a suitable interpolant of the particle positions, and $\tilde{\boldsymbol{v}}$ is the corresponding velocity interpolant. These interpolants can be also viewed as continuum-mechanical quantities: $\tilde{\boldsymbol{q}}$ is the deformation map, and $\tilde{\boldsymbol{v}}$ is the continuum microscale velocity. Since $\tilde{\boldsymbol{q}}$ is interplant, it is not uniquely defend by the particle positions. Provided the underlying ODEs (2.1), (2.2) have the uniqueness property, it should be possible to choose an interpolant such that $\tilde{\boldsymbol{q}}$ is invertible. The inverse deformation map $(\tilde{\boldsymbol{q}})^{-1}$, or "back-to-labels" map, as it is known in the fluid mechanics literature, plays an important role in the method via the Jacobian

$$J = \left|\det \nabla (\tilde{\boldsymbol{q}})^{-1}\right|.$$

In general, integrals in (3.1), (3.2) approximate sums up to a discretization error, but choosing piecewise linear interpolants one can obtain the exact equality. Note also the linear convolution structure of the $\boldsymbol{y}$-integrals in (3.1) and (3.2). We refer to [28] for more details.

3.2.2 | Stress

Here we derive two different approximations for the interaction stress. The first one works best when the number of particles within the range of the potential U is sufficiently large compared with a typical interparticle distance. This would be the case when the majority of particles interacts with sufficiently large number of other particles. Physically this corresponds to dense media such as solids and liquids. Mathematically this implies that discrete sums (2.11), (2.12) in the definition of the stress can be closely approximated by integrals if one interprets these sums as integral quadratures.

To approximate the interaction stress $\boldsymbol{T}^\eta_{(int)}$ in this case, we write $\boldsymbol{q}_i = \tilde{\boldsymbol{q}}(t, \boldsymbol{X}_1)$, $\boldsymbol{q}_j = \tilde{\boldsymbol{q}}(t, \boldsymbol{X}_2)$, and approximate the double sum in (2.12) by the double integral with respect to $\boldsymbol{X}_1$, $\boldsymbol{X}_2$. Then using the force equation (2.5) and changing variables of integration to $\boldsymbol{y}_l = \tilde{\boldsymbol{q}}(t, \boldsymbol{X}_l)$, $l = 1, 2$, we find

$$\boldsymbol{T}^\eta_{(int)}(t, \boldsymbol{x}) = \frac{N}{\varepsilon |\Omega|^2} \int U'\left(\frac{|\boldsymbol{y}_1 - \boldsymbol{y}_2|}{\varepsilon}\right) \frac{(\boldsymbol{y}_2 - \boldsymbol{y}_1) \otimes (\boldsymbol{y}_2 - \boldsymbol{y}_1)}{|\boldsymbol{y}_1 - \boldsymbol{y}_2|} \Psi_\eta(\boldsymbol{x}, \boldsymbol{y}_1, \boldsymbol{y}_2) J(t, \boldsymbol{y}_1) J(t, \boldsymbol{y}_2) d\boldsymbol{y}_1 d\boldsymbol{y}_2, \tag{3.3}$$

where

$$\Psi_\eta(\boldsymbol{x}, \boldsymbol{y}_1, \boldsymbol{y}_2) = \int_0^1 \psi_\eta(\boldsymbol{x} - s\boldsymbol{y}_1 - (1-s)\boldsymbol{y}_2) ds.$$

Next, we change variables again to

$$\boldsymbol{R} = \frac{\boldsymbol{y}_1 + \boldsymbol{y}_2}{2}, \qquad \boldsymbol{\rho} = \frac{\boldsymbol{y}_1 - \boldsymbol{y}_2}{\varepsilon},$$

take into account that Jacobian of this transformation is ε^d, and obtain

$$\boldsymbol{T}^\eta_{(int)}(t, \boldsymbol{x}) = \frac{1}{|\Omega|^2} \int U'(|\boldsymbol{\rho}|) \frac{\boldsymbol{\rho} \otimes \boldsymbol{\rho}}{|\boldsymbol{\rho}|} \psi_\eta(\boldsymbol{x} - \boldsymbol{R}) \boldsymbol{J}(t, \boldsymbol{R} + \frac{\varepsilon}{2}\boldsymbol{\rho}) \boldsymbol{J}(t, \boldsymbol{R} - \frac{\varepsilon}{2}\boldsymbol{\rho}) d\boldsymbol{R}\, d\boldsymbol{\rho}, \tag{3.4}$$

where we have approximated

$$\Psi_\eta(\boldsymbol{x}, \boldsymbol{R}, \boldsymbol{\rho}) = \int_0^1 \psi_\eta(\boldsymbol{x} - \boldsymbol{R} - \boldsymbol{\rho}(s - 1/2)\varepsilon) ds \approx \lim_{\varepsilon \to 0} \int_0^1 \psi_\eta(\boldsymbol{x} - \boldsymbol{R} - \boldsymbol{\rho}(s - 1/2)\varepsilon) ds = \psi_\eta(\boldsymbol{x} - \boldsymbol{R}). \tag{3.5}$$

Here the variable R varies over the domain Ω whereas variable ρ varies either over the whole space, in which case it is assumed that U' decays sufficiently fast at infinity to ensure integrability of the integral in (3.3), or if U' is truncated then ρ varies on the support of U'.

Equation (3.4) expresses the interaction stress as a non-linear integral operator acting on the Jacobian. This operator is a composition of the shifted multiplication $\boldsymbol{J}(t, \boldsymbol{R}) \to \boldsymbol{J}(t, \boldsymbol{R} + \frac{\varepsilon}{2}\rho)\boldsymbol{J}(t, \boldsymbol{R} - \frac{\varepsilon}{2}\boldsymbol{\rho})$, $\boldsymbol{R}$-convolution with ψ_η, and $\boldsymbol{\rho}$-integration with the weight $|\boldsymbol{\rho}|^{-1}\boldsymbol{\rho} \otimes \boldsymbol{\rho}\, U'(|\boldsymbol{\rho}|)$.

The second approximation is more suitable for problems for which the number of interacting neighbors is bounded above by a number that is known a priori. This situation occurs most often in lattice problems. Here we emphasize that for this type of approximation to work, a lattice does not have to be periodic. Often, the interaction potential in such problems is non-integrable (e. g. quadratic) at infinity, so that the potential in the first approximation has to be truncated for the integral in (3.4) to converge. Truncation needs to be done carefully to avoid large errors, and it is not always clear how to do such a truncation. This is a reason for developing the second approximation instead of modifying the first one.

For such problems, it is useful to have a different approximation for $\boldsymbol{T}^\eta_{(int)}$. For simplicity, we consider only the one-dimensional case. Suppose that a particle i interacts with neighbors $i-k, i-k+1, \dots, i-1, i+1, \dots, i+k$ where $k > 0$ is fixed. The interaction stress equation can be written as

$$T^\eta_{(int)} = \sum_{i=1}^{N} \sum_{l=1}^{k} U'\left(\frac{|q_{i+l} - q_i|}{\varepsilon}\right) |q_{i+l} - q_i| \int_0^1 \psi_\eta(x - sq_{i+l} - (1-s)q_i) ds. \tag{3.6}$$

To avoid double counting of interacting pairs, we included only the terms corresponding to $j > i$, $j = i + l$, $l = 1, 2, \dots, k$.

Next, approximate q_{i+l}:

$$q_{i+l} \approx q_i + h \sum_{m=0}^{l-1} \tilde{q}'_{i+l} \approx q_i + hl\tilde{q}'_i, \tag{3.7}$$

where $h = \varepsilon L$, and $\tilde{q}' > 0$ is the derivative of the position interpolant $\tilde{q}(t, X)$ with respect to X. Note that $\tilde{q}'$ can be in principle recovered from the knowledge of $\overline{\rho}^\eta$, since the average density is a convolution with $\boldsymbol{J}$, and

$$\boldsymbol{J}(t, y) = \frac{1}{\tilde{q}'}(t, \tilde{q}^{-1}(t, y)), \qquad \tilde{q}'(t, X) = \frac{1}{\boldsymbol{J}}(t, \tilde{q}(t, X)). \tag{3.8}$$

Substituting this into (3.6) we have

$$T^\eta_{(int)} \approx h \sum_{i=1}^{N} \sum_{l=1}^{k} U'\left(Ll\tilde{q}'_i\right) l\tilde{q}'_i \int_0^1 \psi_\eta(x - q_i - shl\tilde{q}'_i) ds \tag{3.9}$$

$$\approx \int_0^L \sum_{l=1}^{k} U'\left(Ll\tilde{q}'(t, X)\right) l\tilde{q}'(t, X) \int_0^1 \psi_\eta(x - \tilde{q}(t, X) - shl\tilde{q}'(t, X)) ds\, dX. \tag{3.10}$$

Changing the variable $y = \tilde{q}(t, X)$ and using (3.8) we arrive at

$$T^{\eta}_{(int)} \approx \int_0^L \sum_{l=1}^{k} lU'\left(Ll\frac{1}{J}(t,y)\right)\left(\int_0^1 \psi_\eta\left(x - y - \frac{shl}{J(t,y)}\right) ds\right) dy. \tag{3.11}$$

Similarly to (3.5), the integral with respect to s can be approximated by $\psi_\eta(x-y)$ provided J is bounded pointwise independent of N.

Remarks. 1. A special case of (3.11) with $k = 1$ was derived in[28]. The equation in[28] has a different sign because of a slightly different definition of the force used in that article.

2. The multi-dimensional analog of (3.11) can be derived in the same manner. The main difference lies in the fact that (3.8) is not available in higher dimensions. We still can reconstruct J, but what we need is the deformation gradient. It can be obtained indirectly, by recovering J and $\tilde{\boldsymbol{v}}J$ from, respectively, $\overline{\rho}^{\eta}$ and $\overline{\rho}^{\eta}\overline{\boldsymbol{v}}^{\eta}$. That would allow calculation of the microscale velocity $\tilde{\boldsymbol{v}}$. Then we could recover the microscale deformation map $\tilde{\boldsymbol{q}}$ and its gradient from the kinematic equation $\partial_t\tilde{\boldsymbol{q}}(t, \boldsymbol{X}) = \tilde{\boldsymbol{v}}(t, \tilde{\boldsymbol{q}}(t, \boldsymbol{X}))$.

An approximation of the convective stress can be obtained in a similar fashion. The procedure is easier because the convective stress is a sum of terms that depend only on the position and velocity of a single particle. Therefore we list only the final result

$$\boldsymbol{T}^{\eta}_{(c)}(t, \boldsymbol{x}) \approx -\frac{M}{|\Omega|}\int_{\Omega} (\tilde{\boldsymbol{v}}(t, \boldsymbol{y}) - \overline{\boldsymbol{v}}^{\eta}(t, \boldsymbol{x},)) \otimes (\tilde{\boldsymbol{v}}(t, \boldsymbol{y}) - \overline{\boldsymbol{v}}^{\eta}(\boldsymbol{x}, t))\psi_\eta(\boldsymbol{x} - \boldsymbol{y})\boldsymbol{J}(t, \boldsymbol{y})d\boldsymbol{y}. \tag{3.12}$$

Equations (3.4), (3.11) and (3.12) show that stress can be written as on operator acting on J and $\tilde{\boldsymbol{v}}$. According to (3.1) and (3.2), these functions can be recovered from the averages using a suitable approximate deconvolution.

3.3 | Regularized deconvolutions

Since ψ_η is smooth, the convolution operator

$$R_\eta[g](\boldsymbol{x}) = \int \psi_\eta(\boldsymbol{x} - \boldsymbol{y})g(\boldsymbol{y})d\boldsymbol{y} \tag{3.13}$$

is compact in $L^2(\Omega)$. A compact operator cannot have a bounded inverse unless the range of R_η is finite-dimensional (see e.g. in[17] Thm 1.17). As a consequence, the inversion problem is unstable. If the difference between two right hand sides is small, then the difference between the corresponding solutions may be large. Such *ill-posed problems* are well investigated analytically and numerically (see, e. g.[16,21,17,19,20,18]). Stable approximate solutions of the integral equation

$$R_\eta[g] = \overline{g}^{\eta} \tag{3.14}$$

can be obtained by using regularization. Some numerical regularization methods are described in C. Below, we assume that a regularized approximate inverse Q^{α}_{η} is chosen, and write

$$g \approx Q^{\alpha}_{\eta}[\overline{g}^{\eta}]. \tag{3.15}$$

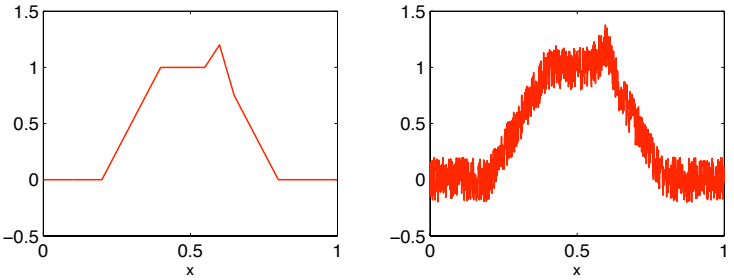

FIGURE 1 Left panel: mesoscale and sub-filter scale features g; right panel: exact solution g with a uniformly distributed noise added.

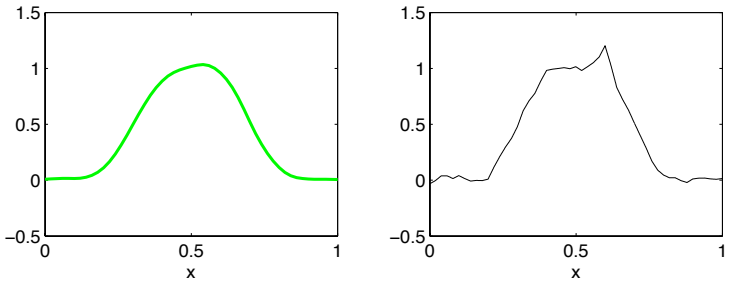

FIGURE 2 Left panel: the average $\overline{g}^{\eta}$ (right hand side of the integral equation (3.14)); right panel: reconstructed approximation of g.

An example of deconvolution is shown in Figs. 1 and 2 . In the first of these plots depicted in Fig. 1 we show the exact solution g. It is constructed by first choosing a profile to be reconstructed (left panel), and then adding noise (right panel). The graph in the left panel contains a mesoscale feature (trapezoidal impulse in the center), and a sub-filter scale feature (smaller triangular impulse on top of the trapezoid). The noise contains multiple features on smaller length scales. The right hand side vector $\overline{g}$, computed by applying the convolution operator R_η to g from the right panel of Fig. 1 , is shown in the left panel of Fig. 2 . All features except the largest appear to be smeared. The right panel in Fig. 2 shows the reconstruction. The noise is largely filtered out but the sub-filter feature is clearly visible. For more details on numerical implementation of regularized deconvolution methods, please see C.

3.4 | Closed form approximation of the stress

The closure is achieved by replacing J, $\tilde{\boldsymbol{v}}$ in (3.4) (or (3.11)) and (3.12) with the deconvoluted approximations obtained by approximately solving the integral equations (3.1) and (3.2):

$$J \approx \frac{|\Omega|}{M} Q_\eta^\alpha[\overline{\rho}^\eta], \qquad \tilde{\boldsymbol{v}} \approx \frac{Q_\eta^\alpha[\overline{\rho}^\eta \overline{\boldsymbol{v}}^\eta]}{Q_\eta^\alpha[\overline{\rho}^\eta]}, \tag{3.16}$$

where Q_η^α is a regularized approximate inverse to the convolution operator R_η (see 3.13), (3.15)). The result is the approximate stress $\overline{\boldsymbol{T}}^{\eta^\eta} = \overline{\boldsymbol{T}}^\eta_{(c)} + \overline{\boldsymbol{T}}^\eta_{(int)}$ given by a non-linear integral operator acting on $\overline{\rho}^\eta$, $\overline{\rho}^\eta \overline{\boldsymbol{v}}^\eta$.

The approximation error $e = \boldsymbol{T}^\eta - \overline{\boldsymbol{T}}^\eta$ can be written as

$$e = \mathcal{E}_d(\delta) + \mathcal{E}_i, \tag{3.17}$$

where $\mathcal{E}_d$ is error of replacing the exact J, $\tilde{\boldsymbol{v}}$ with (3.16) in the integral formulas (3.4), (3.12), and $\mathcal{E}_i$ comes from replacing the sums in the definition of $\boldsymbol{T}^\eta$ with the integrals (3.4), (3.12).

Denote by δ an upper bound on the norm of the error in approximation of the exact averages in (2.6), (2.7) with their integral approximations (3.1), (3.2). Then clearly error $\mathcal{E}_d$ depends on δ. Since filtered regularization methods (see C and formulas (C2) and (C3)) are used to approximate J and $\tilde{\boldsymbol{v}}$, the error $\mathcal{E}_d$ is a continuous function of δ and $\lim_{\delta\to 0} \mathcal{E}_d(\delta) = 0$. The size of δ can be controlled by choosing interpolants $\tilde{\boldsymbol{q}}$, $\tilde{\boldsymbol{v}}$. In theory, δ can be made zero by choosing the interpolants in such a way that definitions (2.6), (2.7) are exact midpoint quadratures of the corresponding integrals. In practice, however, δ would still be on the order of the machine round-off error, and regularization would be still needed.

Next, consider $\mathcal{E}_i$. If equation (3.4) is used, this error can also be reduced by a suitable choice of interpolants. The situation is more complicated for (3.11) because of the use of an additional approximation (3.7). So, from the point of view of error control, using (3.4) should be preferred. However, equation (3.11) is closer to conventional phenomenological models, and gives reasonably good results for small k.

Finally, we note that the above discussion does not include the error of numerical implementation of the constitutive equations. This error would occur if one wishes to have the operation count per time step to scale as $O(N)$ or better. This would require discretizing the averages on a coarser mesoscopic mesh. The integrals in the constitutive equations would be represented by

coarse quadratures, and the resulting error would depend on the mesoscopic mesh size. Partial error estimates for the interaction stress are presented in [34].

4 | MESOSCOPIC CONTINUUM EQUATIONS FOR FPU CHAINS

In this section we consider Hamiltonian chains of oscillators that consists of N identical particles. The domain Ω is an interval $(0, L)$. Particle positions, denoted by $q_j = q_j(t)$, $j = 1, \dots, N$, satisfy

$$0 < q_1 < q_2 < \dots < q_N < L$$

at all times, i.e. the particles cannot occupy the same position or jump over each other.

In this section we suppose that each particle interacts with k nearest neighbors. The interaction force is generated by the pair potential U. The integral approximations of the stress are given by (3.11), (3.12). These equations contain two microscale quantities: J and $\tilde{v}$. From (3.1), (3.2) it is clear that $\overline{\rho}^\eta$ and $\overline{v}^\eta$ are obtained by applying R_η to, respectively, J and $J\tilde{v}$. Application of a regularized deconvolution Q_η^α yields integral approximations

$$J \approx \frac{L}{M} Q_\eta^\alpha[\overline{\rho}^\eta], \qquad \tilde{v} \approx \frac{Q_\eta^\alpha[\overline{\rho}^\eta \overline{v}^\eta]}{Q_\eta^\alpha[\overline{\rho}^\eta]}. \tag{4.1}$$

Inserting these approximation into (3.11) and (3.12) we obtain the closed form mesoscopic continuum equations

$$\partial_t \overline{\rho}^\eta + \partial_x(\overline{\rho}^\eta \overline{v}^\eta) = 0, \tag{4.2}$$

$$\partial_t(\overline{\rho}^\eta \overline{v}^\eta) + \partial_x\left(\overline{\rho}^\eta (\overline{v}^\eta)^2\right) - \partial_x(\overline{T}^\eta_{(c)} + \overline{T}^\eta_{(int)}) = 0, \tag{4.3}$$

where $\overline{T}^\eta_{(c)}, \overline{T}^\eta_{(int)}$ are given by

$$\overline{T}^\eta_{(c)} = -\int_0^L \left(\frac{Q_\eta^\alpha[\overline{\rho}^\eta \overline{v}^\eta]}{Q_\eta^\alpha[\overline{\rho}^\eta]}(t,y) - \overline{v}^\eta(t,x) \right)^2 \psi_\eta(x-y)(t,y) Q_\eta^\alpha[\overline{\rho}^\eta](t,y) dy, \tag{4.4}$$

$$\overline{T}^\eta_{(int)} = \int_0^L \sum_{l=1}^k U'\left(\frac{Ml}{Q_\eta^\alpha[\overline{\rho}^\eta](t,y)} \right) \int_0^1 \psi_\eta\left(x - y - \varepsilon \frac{Msl}{Q_\eta^\alpha[\overline{\rho}^\eta](t,y)} \right) ds\, dy. \tag{4.5}$$

The choice of the operator Q_η^α is not unique: it depends on the specifics of the regularization method and the chosen value of the regularization parameter. For classical regularization schemes such as Landweber [31], Tikhonov, and truncated SVD (see e.g. [17]), this operator is a convolution with the kernel $Q(x)$ that can be described explicitly in terms of the singular values and singular vectors of R_η (see [17] for details). An explicit kernel description in terms of ψ_η is available for iterative methods such as Landweber's.

In [28] we studied a special case of (4.1) corresponding to the Landweber approximation with $n = 0$, given by Eq. (C4) in Appendix C. In that case, called zero-order closure, Q is the identity operator. This means that

$$J \approx \frac{L}{M} \overline{\rho}^\eta, \qquad \tilde{v} \approx \overline{v}^\eta. \tag{4.6}$$

Note that in practice the left hand side would be discretized on a fine mesh with size $h = \varepsilon L$, while the right hand side would be resolved on a coarser mesh with size $\Delta \gg h$. To make sense of (4.6), one should interpolate $\overline{\rho}^\eta, \overline{v}^\eta$ to the fine mesh. Interpolation can be viewed as a way to assign particle positions and velocities based on the knowledge of the averages. Choosing a piecewise constant interpolant yields a well known quasi-continuum approximation [32,33]. Indeed, in this case all particles located in a meso-cell would move with the average velocity of the center of that cell. Thus, deconvolution closure is a natural extension of the quasi-continuum method.

5 | LOCAL CONSTITUTIVE EQUATIONS FOR INTERACTION STRESS

The constitutive equation (4.5) is non-local in space. This is in contrast to classical phenomenological equations given by local functions of kinematic variables and temperature. In this section we investigate the possibility of approximating the interaction

stress given by equation (4.5) by a function of the average density. Since in one dimension knowledge of density is equivalent to the knowledge of the average deformation gradient, one can also pose the above question in terms of the deformation gradient. Local constitutive equations can be helpful in linking the present approach with standard phenomenological models. Another desirable feature of local equations is their comparative simplicity and ease of use.

In this section we consider only the case $k = 1$ (nearest neighbor interactions). Since ψ_η is slowly varying, and $\varepsilon \ll \eta$, equation (4.5) can be simplified by replacing the integral with respect to s by $\psi_\eta(x - y)$. Then, letting $F(t) = U'\left(\frac{L}{t}\right)$, we can write

$$T^\eta_{(int)} \approx R_\eta[F(J)] = \int F(J(y))\psi_\eta(x - y)dy.$$

Standard results on mollifiers imply that $R_\eta[F(J)]$ converges to $F(J)$ as $\eta \to 0$. This seems to provide a simple answer, but this answer is unsatisfactory. The Jacobian J is a micro-scale function that would be impossible to evaluate without solving the underlying ODEs. Another reason has to do with scale separation. The limit $\eta \to 0$ corresponds to averaging over infinitesimally small volume while N and ε are being fixed. In the limit, meso-scale spatial averages are replaced with highly oscillatory, non-observable dynamical functions such as $\sum_{i=1}^N m_i\delta(\boldsymbol{x} - \boldsymbol{q}_i)$.

Therefore we focus on a different question. Given a fixed $\eta > 0$, is it possible to approximate $R_\eta[F(J)]$ by a function G of $\overline{\rho}^\eta$?

Since many situations of practical interest involve simulation, it is natural to consider the above question in the discretized setting. Thus, suppose that $T_{(int)}$ should be computed at the points of x_β of the meso-scale mesh with η. The quantity to be approximated is a vector with components

$$R_F(J)_\beta = R_\eta[F(J)](x_\beta) = \int F(J(y))\psi_\eta(x_\beta - y)dy. \tag{5.1}$$

To simplify calculations, consider a representative model window function $\psi(t)$ given by the characteristic function of $[-1/2, 1/2]$. Then $\psi_\eta(x_\beta - y)$ is the characteristic function of an interval (coarse mesh cell) $\widehat{I}_\beta = \left(x_\beta - \frac{\eta}{2}, x_\beta + \frac{\eta}{2}\right)$. Averaging is thus carried out on non-overlapping intervals $\widehat{I}_\beta$. The input data consists of mesh values

$$\overline{\rho}^\eta_\beta = \overline{\rho}^\eta(x_\beta) = \frac{L}{M}\int J(y)\psi_\eta(x_\beta - y)dy = \frac{L}{M}\int\limits_{\widehat{I}_\beta} J(y)dy = \frac{L}{M}\overline{J}_\beta \tag{5.2}$$

where $\overline{J}_\beta$ is the local average of J. The function J, considered to be unknown, is resolved on a fine scale (microscopic) mesh with points y_j and mesh spacing $\epsilon \ll \eta$, and mesh cells I_j. For simplicity, assume that each $\widehat{I}_\beta$ contains η/ε of I_j, and that η/ε is an integer.

We can identify the vector of mesh values J_j of the Jacobian with the piecewise constant function

$$J(y) = \sum_j J_j\psi\left(\frac{y - y_j}{\epsilon}\right). \tag{5.3}$$

Combining (5.3) and (5.1) yields

$$\int F\left(\sum_j J_j\psi\left(\frac{x - y_j}{\epsilon}\right)\right)\psi_\eta(x_\beta - y)dy = \sum_{j\in J(\beta)}\int\limits_{I_j} F(J_j)\psi_\eta(x_\beta - y)dy$$

$$= \sum_{j\in J(\beta)}\frac{1}{\eta}\int F(J_j)\psi\left(\frac{y - y_j}{\epsilon}\right)\psi\left(\frac{x_\beta - y}{\eta}\right)dy = \frac{\epsilon}{\eta}\sum_{j\in J(\beta)} F(J_j),$$

where $J(\beta)$ is the index set of I_j contained in $\widehat{I}_\beta$. Next, writing

$$F(J_j) = F\left(\bar{J}_\beta + (J_j - \bar{J}_\beta)\right)$$

and using Taylor expansion of $F(J_j)$ about $\bar{J}_\beta$ we find

$$F(J_j) = F(\bar{J}_\beta) + \sum_{k=1}^n \frac{F^{(k)}(\bar{J}_\beta)}{k!}(J_j - \bar{J}_\beta)^k + R_n(J_j - \bar{J}_\beta).$$

Thus,

$$\int F\Big(J(y)\Big)\psi_\eta(x_\beta - y)dy = F(\bar{J}_\beta)) + \frac{\epsilon}{\eta}\sum_{k=1}^n\sum_{j\in J(\beta)}\frac{F^{(k)}(\bar{J}_\beta)}{k!}(J_j - \bar{J}_\beta)^k + \frac{\epsilon}{\eta}\sum_{j\in J(\beta)} R_n(J_j - \bar{J}_\beta)$$

$$= F(\bar{J}_\beta) + \sum_{k=1}^{n} \frac{F^{(k)}(J(\bar{\beta}))}{k!} \left(\frac{\epsilon}{\eta} \sum_{j \in J_\beta} (J_j - J(\bar{\beta}))^k \right) + \frac{\epsilon}{\eta} \sum_{j \in J(\beta)} R_n(J_j - \bar{J}_\beta).$$

Next, observe that

$$\sum_{j \in J(\beta)} J_j - \bar{J}_\beta = 0, \tag{5.4}$$

so that

$$\int F(J(y))\, \psi_\eta(x_\beta - y) dy = F(\bar{J}_\beta) + \sum_{k=2}^{n} \frac{F^{(k)}(\bar{J}_\beta)}{k!} \left[\frac{\epsilon}{\eta} \sum_{j \in J(\beta)} (J_j - \bar{J}_\beta)^k \right] + \frac{\epsilon}{\eta} \sum_{j \in J(\beta)} R_n(J_j - \bar{J}_\beta). \tag{5.5}$$

This shows that complete knowledge of J_j is unnecessary for constructing an accurate approximation of the interaction stress. We only need to know a finite number of moments

$$M_{k,\beta} = \frac{\epsilon}{\eta} \sum_{j \in J(\beta)} (J_j - \bar{J}_\beta)^k. \tag{5.6}$$

Knowledge of $M_{k,\beta}$ is not equivalent to knowledge of all J_j, since $M_{k,\beta}$ depend on the number of times a particular value of J_j occurs in $\widehat{I}_\beta$, but not on the actual locations of these values. So, the information contained in $M_{k,\beta}$ is intermediate between the limited meso-scale information contained in $\bar{J}_\beta$, and the complete micro-scale information contained in $J(y)$.

Relation (5.5) shows that in general there is no function G such that $G(\overline{\rho}^\eta_\beta) = R_F(J)_\beta$. Indeed, fluctuations are obliterated by averaging, as (5.4) indicates, and thus it is possible for two cells to have the same average $\overline{J}$, but different values of $M_{k,\beta}$. In the continuum setting, a proper choice of the window function ensures that J can be, in principle, uniquely reconstructed from $\overline{J}$. Exact reconstruction is not feasible because of instability, but even such abstract uniqueness is absent in the discretized setting. Thus, discretization leads to additional loss of information compared with continuum setting. Therefore $G(\overline{\rho}^\eta_\beta) = R_F(J)_\beta$ is possible only if J does not fluctuate on scales smaller than η. In that case $J(y_j) = \overline{J}(y_j)$ for each y_j, all $M_{k,\beta}$ are zero, and

$$G(\overline{\rho}^\eta) = F\left(\frac{L}{M} \overline{\rho}^\eta \right).$$

For finite η, generic constitutive equations are non-local. They may be approximated by local equations if fluctuations are suitably small compared with the mean values $\overline{J}_\beta$. A more general condition is that fluctuations are nearly constant in time and have nearly the same distribution at each $\widehat{I}_\beta$. Otherwise, error associated with using local constitutive equations can be large.

The simplest approximation that takes fluctuations into account is obtained when $M_{2,\beta} \approx \theta$ for all β, and higher-order moments can be neglected. Then

$$G(\overline{\rho}^\eta) = \left(F + \frac{1}{2}\theta F'' \right) \left(\frac{L}{M} \overline{\rho}^\eta \right). \tag{5.7}$$

The above empirical statistics is a natural extension of the deconvolution closure. The connection between the two is as follows. It is often advantageous to increase η because this produces less oscillatory averages. At the same time, to increase numerical fidelity, one might wish to use a finer mesh of size $\Delta < \eta$. In that case the intervals $\widehat{I}_\beta$ overlap. Then deconvolution can be used to reconstruct unknown averages on the finer scale Δ from the available averages on the coarser scale η. The Δ-averages can be used as approximations of the micro-scale quantities. For example, $\overline{\rho}^\eta$ in equation (5.7) should be replaced with $\overline{\rho}^\Delta = Q^\alpha_\eta[\overline{\rho}^\eta]$. Then the local constitutive equation takes the form

$$T_{(int)} \approx \left(F + \frac{1}{2}\theta F'' \right) \left(\frac{L}{M} Q^\alpha_\eta[\overline{\rho}^\eta] \right).$$

6 | NUMERICAL EXPERIMENTS

In this section, we test the performance of the proposed method using two different potentials: the classical Lennard-Jones potential and a potential that resembles a Hertz potential employed in modeling of granular materials. The exact particle positions and velocities are obtained by solving the ODEs (2.1), (2.2) with various initial conditions. These exact solutions are used to generate the Jacobian, the average density, average velocity and the exact stress. Then we employ the regularized deconvolution technique to approximate the Jacobian and microscopic velocity, which are then used to approximate the stress. The exact and approximated quantities are compared to analyze the accuracy of the proposed closure method.

6.1 | Lennard-Jones chain

In this example, we simulate a chain of particles interacting with Lennard-Jones potential plotted in left panel of Fig. B2 and defined in (B1) in the Appendix B. The initial positions are equally spaced with $q_j^0 = (j-1/2)h$, $j = 1, \dots, N$. We consider two different sets of initial velocities shown in Fig. 3 . The left panel contains a mesoscale feature (the larger peak), and a sub-filter scale feature (the smaller peak). The right panel shows the same initial velocity but with added noise. The noise is a realization of a uniformly distributed random variable. In the sequel, we refer to the first initial condition as deterministic, while the second initial condition is called noisy.

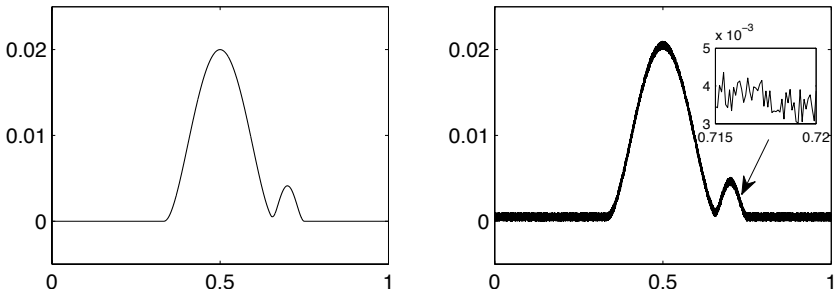

FIGURE 3 Left panel: deterministic initial velocity; right panel: noisy initial velocity.

In Fig. 4 , we show exact and reconstructed Jacobians in both deterministic and noise cases. The exact Jacobians in these two cases are different, but both reconstructions have oscillatory features. The similarity may be due to the built-in filtering in the deconvolution algorithm. This filtering is rather soft, since the reconstructed Jacobians contain oscillatory artifacts on scales comparable with the microscale. The amplitude of the artifacts is under control, so that the relative l_∞ error does not exceed 0.3%. This shows that the reconstruction is stable.

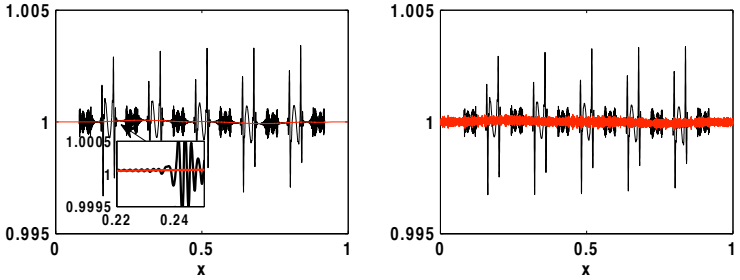

FIGURE 4 Left panel: reconstruction of the Jacobian J in the deterministic case; right panel: noisy case. Red/grey curves represent the exact solutions, black curves - their reconstruction.

The velocity reconstruction is shown in Fig. 5 . The average velocities in the noisy and deterministic case are nearly identical. Averaging obliterates sub-filter scale features, but the deconvolution algorithm recovers these features well as shown in the insert in the left panel of Fig. 5 , where one can clearly see that the reconstructed velocity is much closer to the exact velocity than the average velocity. In the noisy case, deconvolution still recovers sub-filter scale features, but the high frequency component of the noise is filtered out. As a consequence, the reconstructed velocity is closer to the average velocity than to the exact one. In Fig. 6 , we show the exact convective stress $T^\eta_{(c)}$ and its closed form approximation $\overline{T}^\eta_{(c)}$ computed from the equation (4.4). We see that the approximation quality is better in the deterministic case. In the noisy case, the main features of the stress are still well recovered, despite a significant difference between the exact and reconstructed velocities (Fig. 5).

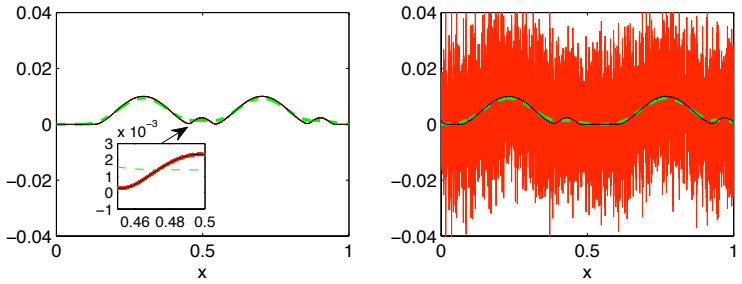

FIGURE 5 Left panel: reconstruction of the velocity $\tilde{v}$ in the deterministic case; right panel: noisy case. On both panels the exact velocity is shown in red (dark grey) thin solid line, the average velocity in green (light grey) dashed line, and the reconstructed velocity in black solid line.

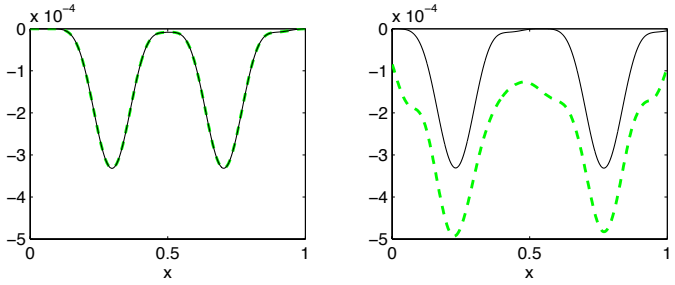

FIGURE 6 Exact convective stress $T^{\eta}_{(c)}$ (green (grey) dashed line), and the approximation $\overline{T}^{\eta}_{(c)}$ (black solid line). Left panel: deterministic case; right panel: noisy case.

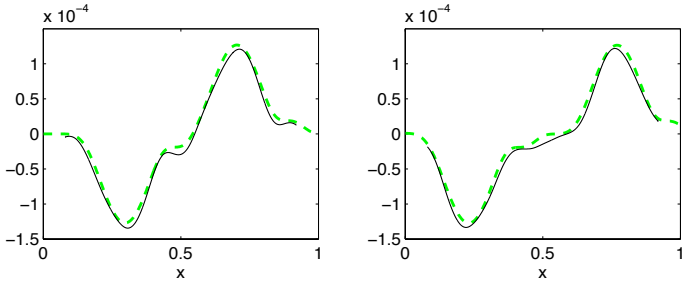

FIGURE 7 Exact interaction stress $T^{\eta}_{(int)}$ (green (grey) dashed line), and the approximation $\overline{T}^{\eta}_{(int)}$ (black solid line). Left panel: deterministic case; right panel: noisy case.

The interaction stress $T^{\eta}_{(int)}$ and its closed form approximation $\overline{T}^{\eta}_{(int)}$ (eq. (4.5)) are shown in Fig. 7 . The approximation quality is about the same in both cases. According to (4.5), the accuracy depends on the quality of the reconstruction of the Jacobian. Comparison of Fig. 4 and Fig. 7 shows that the high frequency artifacts and noise in the Jacobian are smoothed out by averaging in (4.5). This is important since the interaction stress depends non-linearly on the Jacobian. In contrast to the linear case, non-linear averaging functionals may exhibit sensitivity to oscillations in the input function (in this case, Jacobian). Non-linearity induces dispersion, and this may result in transfer of the input's high frequency content into the low frequency content of the functional. In the present case, this does not happen. We conjecture that for generic molecular potentials such as Lennard-Jones, and for a broad class of initial conditions, the stress functional has the self-averaging property, meaning that the effect of dispersion is weak compared to the filtering effect of convolution.

6.2 | Granular acoustics

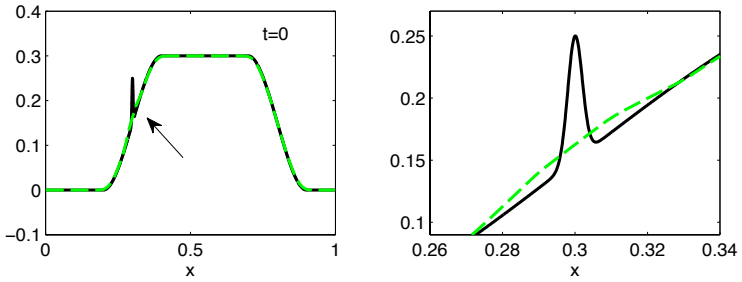

FIGURE 8 Initial microscopic velocity v^0 (black solid curve) defined in (B4), (B5) together with the average velocity $\bar{v}$ (green dashed curve). Left panel: velocities are plotted on the entire domain $[0, 1]$; right panel: zoom-in of velocities on the interval $[0.26, 0.34]$ that contains a sub-filter feature.

In this subsection, we test the method on a chain of particles interacting with a pair potential $U(\xi)$ defined in the Appendix in (B3) and depicted in the right panel of Fig. B2 . The particles represent the centers of spherical granules and the potential resembles a Hertz potential employed in modeling of granular materials. The corresponding force is purely repulsive and has a finite range equal to the equilibrium distance between the neighboring particles.

We solve the system of ODEs (2.1), (2.2) with two different initial conditions and periodic boundary conditions. In both examples, the initial positions q_j are equally spaced on the interval $(0, L)$ at the equilibrium distance $h = L/N$ with $L = 1$ and $N = 10{,}000$. The initial velocity for the first example, shown in Fig. 8 (black curve) and defined in the Appendix (B4), (B5), contains features of different length scales. The size of the larger feature of trapezoidal shape is bigger than ηL (mesoscale or filter scale). The smaller feature is a Gaussian with the standard deviation $0.2\eta L$ (sub-filter scale). At this length scale, the feature is completely obscured by the averaging (green dashed curve) as can be seen in the right panel of Fig. 8 where the velocity is zoomed around $x = 0.3$.

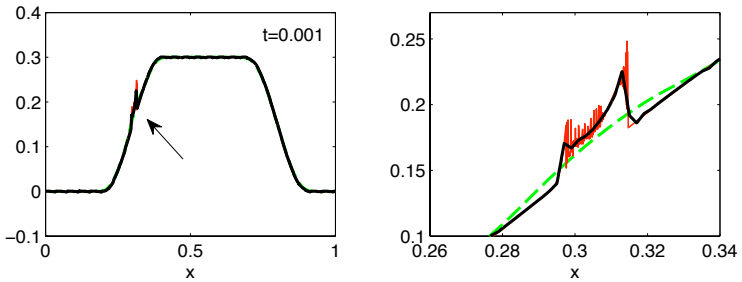

FIGURE 9 Velocity reconstruction: microscopic velocity $\tilde{v}$ (red thin solid curve), reconstructed velocity $\frac{Q_\eta[\overline{\rho}^\eta \overline{v}^\eta]}{Q_\eta[\overline{\rho}^\eta]}$ (black thick solid curve) and average velocity $\bar{v}$ (green dashed curve). Left panel: on the entire domain; right panel: zoom-in of the region that contains a feature due to Gaussian perturbation.

The system of ODEs (2.1), (2.2) is solved numerically until $t = 2.2 \cdot 10^{-2}$ after which the solution develops a shock. First, we test the quality of reconstruction of $\tilde{v}$ and J. Figure 9 compares the exact $\tilde{v}$ (red thin solid curve), its reconstructed approximation $\frac{Q_\eta[\overline{\rho}^\eta \overline{v}^\eta]}{Q_\eta[\overline{\rho}^\eta]}$ (black thick solid curve) and the average $\bar{v}$ (green dashed curve) at $t = 10^{-3}$. The left panel shows that the reconstruction captures the large scale features (left panel) as well as features on the sub-filter scale (right panel). In contrast, the average velocity completely misses the sub-filter scale. In Fig. 10 , we compare the exact microscopic Jacobian J (red thin solid curve) with the reconstructed Jacobian $\frac{L}{M} Q_\eta[\overline{\rho}^\eta]$ (black thick solid curve) and the average scaled density $\frac{L}{M}\rho$ (green dashed curve).

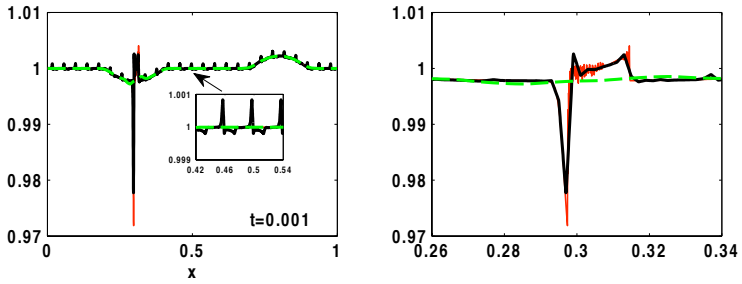

FIGURE 10 Jacobian reconstruction: microscopic Jacobian J (red thin solid curve), reconstructed Jacobian $\frac{L}{M}Q_\eta[\overline{\rho}^\eta]$ (black thick solid curve) and average density $\frac{L}{M}\rho$ (green dashed curve). Left panel: solutions are shown on the entire domain; right panel: zoom-in of the region with sub-filter scale features.

Similar to velocity reconstruction, Fig. 10 indicates that the reconstructed Jacobian is much closer to the exact Jacobian than the average density.

Next we examine how well convective $T^\eta_{(c)}$ and interaction $T^\eta_{(int)}$ stresses are approximated by $\overline{T}^\eta_{(c)}$ and $\overline{T}^\eta_{(int)}$ defined in (4.4), (4.5). The left panel of Fig. 11 indicates that the exact convective stress and its approximation are almost indistinguishable. The right panel of Fig. 11 shows good agreement between the exact interaction stress and its approximation. For comparison, we also plot an approximation using a zero-order closure from[28] shown for convenience in (4.6) that fails to capture sub-filter scale features in both stresses.

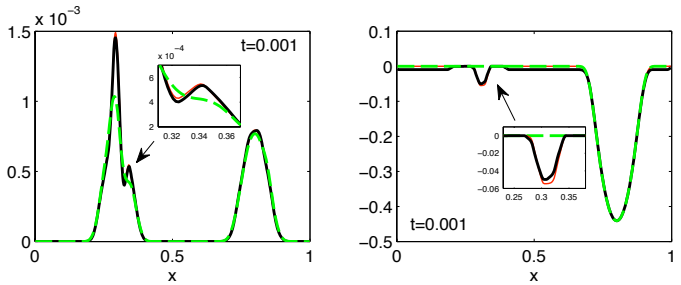

FIGURE 11 Left panel shows convective stresses: exact $T^\eta_{(c)}$ (red thin solid curve), its approximation via reconstruction $\overline{T}^\eta_{(c)}$ (black thick solid curve), and an approximation (green dash curve) using zero-order closure (4.6); right panel: interaction stress $T^\eta_{(int)}$ and its corresponding approximations.

The l_∞-error in approximation of $T^\eta_{(c)}$ by $\overline{T}^\eta_{(c)}$ is between 1.5% and 10% during the simulation time. The error in approximation of $T^\eta_{(int)}$ is smaller and varies from 1.5% to 8%. Computational studies indicate that the error decreases as N increases. Similar findings are reported in[34].

The initial velocity in the second example is the sum of v^{base} defined in (B4) and a sine function with period 0.012, added on the interval $[0, 0.6]$ (see Fig. 12 and formula in (B6) in the Appendix). Simulations were also done until $t = 2.2 \cdot 10^{-2}$. The right panel of Fig. 12 shows that at $t = 0$ the average velocity does not contain oscillations present in the microscopic velocity. Fig. 13 presents graphs of velocity and Jacobian at a representative moment of time, $t = 10^{-3}$. The reconstructed velocity and Jacobian contain main features of their microscopic counterparts while the averages do not.

Fig. 14 depicts the stress. Both convective and interaction exact stresses have sharp transition regions near $x = 0.05$ and $x = 0.6$. Our closed form approximation qualitatively captures these features while a zero-order closure approximation is nearly zero on the entire interval. The error in approximation of the convective stress fluctuates at early times (until $t = 3 \cdot 10^{-3}$) from 15% to 70% and then settles around $35 - 40\%$. The error in the approximation of the interaction stress behaves similarly at early times, then decreases to 10% and levels off. The error in using the zero-order closure is much higher: $75 - 100\%$ for the

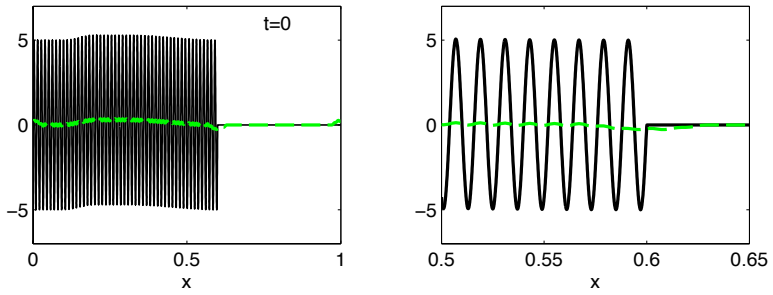

FIGURE 12 Initial velocity with sine perturbation: microscopic velocity v^0 (black solid curve) and average velocity $\bar{v}$ (green dashed curve). Left panel: velocity is shown on the entire domain; right panel: zoom-in of the velocity on the interval $[0.5, 0.65]$.

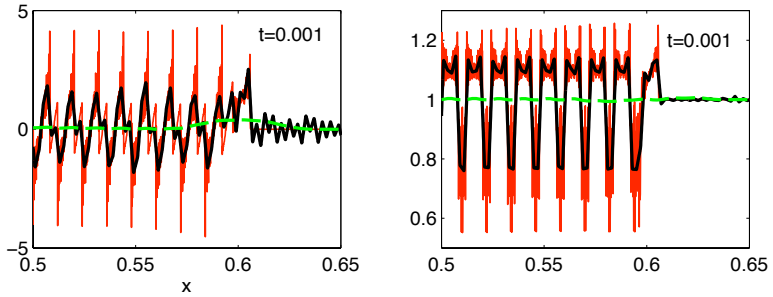

FIGURE 13 Reconstruction of velocity $\tilde{v}$ (left panel); reconstruction of the Jacobian (let panel) at $t = 10^{-3}$. The functions are plotted on the interval $[0.5, 0.65]$ to show details.

convective stress during the entire simulation time and around 100% for the interaction stress until $t = 2 \cdot 10^{-3}$, then it drops to $10 - 15\%$ at $t = 7 \cdot 10^{-3}$, after which the error is about the same as using the reconstruction.

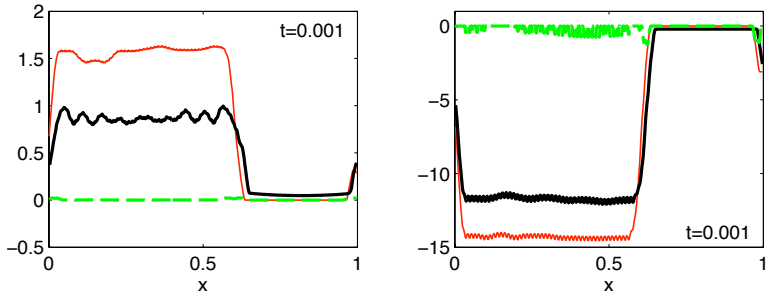

FIGURE 14 Left panel: convective stress; right panel: interaction stress.

Compared to the previous set of initial conditions, the performance of the method seems to be worse. This could be explained by noting that in our numerical experiments the singular vectors are close to the discretizations of the Fourier basis functions (sines and cosines). Thus truncated SVD filtering is similar to the low-pass filtering of Fourier harmonics. The presence of the higher frequency oscillations in the initial conditions creates a strong sub-filter scale peak in the Fourier spectrum of the microscale dynamical functions. This peak can be difficult to capture by a low-pass filtering method. By contrast, the Fourier

spectrum of an isolated Gaussian used in the previous example decreases fast for larger frequencies. Low-pass filtering in that case preserves more information about the original signal.

For more on the performance of the regularized deconvolution method depending of the choice of the averaging window function, the value of the mesoscale resolution parameter, scale separation, the level of truncation of singular values, and the level of spectral filtering of the averages, please see[34].

7 | CONCLUSIONS

We present a method for deriving closed form mesoscale continuum models of large particle systems. The closure construction is based on the following. Non-linear mesoscale averages can be rewritten as linear convolutions of the window function and appropriate microscale dynamical functions. One such function of particular importance is the inverse Jacobian of the microscale flow map associated with a position interpolant. Using the theory of ill-posed problems, we produce stable deconvolution approximations of particle positions and velocities in terms of the average density and average momentum. Closure is achieved by inserting these approximations into the equations for fluxes instead of the actual positions and velocities. The resulting constitutive equations (4.4), (4.5) are non-local in space and non-linear.

In the simplest version of the method, the microscale quantities are approximated by their averages. We studied this approximation in the earlier paper[28]. The results presented there indicate that the simplest approximation works well for systems characterized by (i) small fluctuations of the initial velocity; and (ii) nearly isothermal dynamics. In this article we consider more general initial conditions that contain prominent small scale peaks, significant noise, or high frequency periodic oscillations. Averaging obscures these features to such an extent that the approximation from[28] becomes unsatisfactory. Here we were able to recover such details using non-iterative regularization methods.

We tested the method numerically on two models of FPU-chains: the classical Lennard-Jones chain and the granular acoustics model considered earlier in[28], but with more general initial conditions. The ODEs were solved by the velocity Verlet method, and the obtained particle positions and velocities were used to calculate the average density, linear momentum, and the exact stress. Then we used regularized deconvolution to generate the approximate (reconstructed) Jacobian and velocity. The resulting closed form approximation of the stress agreed well with its exact counterpart.

8 | ACKNOWLEDGMENTS

Work of Lyudmyla Barannyk was supported in part by Amendment No. 005 to Task Order No. 00041 Under Master Task Agreement No. 00042246 Battelle Energy Alliance, LLC (BEA). She would also like to acknowledge the availability of computational resources at Idaho National Laboratory (INL).

□

APPENDIX

A WINDOW FUNCTION

In this paper, we use the following trapezoidal shaped function ψ:

$$\psi(\xi) = \begin{cases} \frac{1}{a+b}, & \text{if} \quad |\xi| \le a, \\ \frac{\xi - b}{a^2 - b^2}, & \text{if} \quad a < \xi < b, \\ -\frac{\xi + b}{a^2 - b^2}, & \text{if} \quad -b < \xi < -a, \\ 0, & \text{if} \quad |\xi| \ge b \end{cases} \tag{A1}$$

with $L = 1$, $a = L/2$, $b = 3L/2$. It can be directly checked that $\int_{-\infty}^{\infty} \psi(\xi) d\xi = \int_{-b}^{b} \psi(\xi) d\xi = 1$. The function ψ is plotted in Fig. A1 .

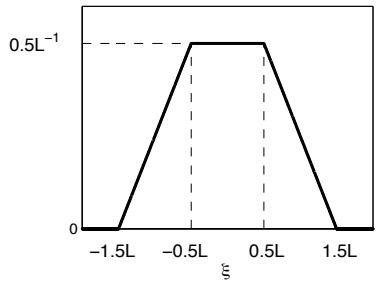

FIGURE A1 The function $\psi(\xi)$.

B POTENTIALS AND INITIAL CONDITIONS

In Section 6, we test the method using two potentials: the first is the Lennard-Jones potential, the second potential is similar to the Hertz potential employed in modeling of granular materials.

B.1 Lennard-Jones

The potential is plotted in the left panel of Fig. B2 and defined by

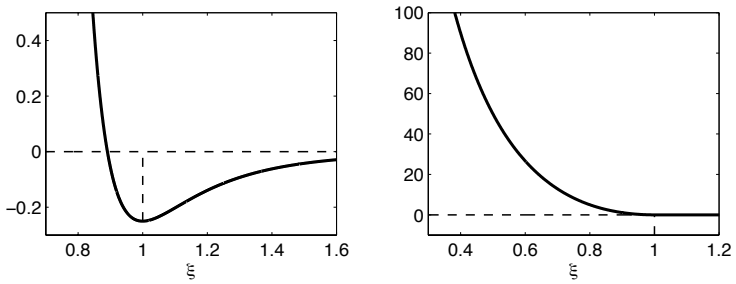

FIGURE B2 Left panel: Lennard-Jones potential; right panel: Hertz type potential.

$$U(\xi) = 4\epsilon \left[\left(\frac{\sigma}{\xi} \right)^{12} - \left(\frac{\sigma}{\xi} \right)^{6} \right], \tag{B1}$$

where $\epsilon = 0.25$ defines the depth of the potential well, σ is the finite distance at which the potential is zero, ξ is the distance between particles. The potential is at a minimum when $\xi = h = 2^{1/6}\sigma$, which determines the choice of σ. The force corresponding to the Lennard-Jones potential is repulsive for distances smaller than h and attractive for distances greater than h.

The initial particles positions in all numerical test problems are equally spaced with step h and defined by $q_j^0 = (j - 1/2)h$, $j = 1, \dots, N$. The initial velocity used in the deterministic case is

$$v(q_j^0) = f(q_j^0) + \lambda \left(q_j^0 - 0.7 \right), \quad j = 1, \dots, N \tag{B2}$$

where

$$f(\xi) = \begin{cases} \frac{1}{50} \left(\xi - \frac{1}{3} \right)^2 \left(\frac{2}{3} - \xi \right)^2 & \text{if} \quad \frac{1}{3} < \xi < \frac{2}{3}, \\ 0 & \text{otherwise.} \end{cases}$$

and

$$\lambda(\xi) = \begin{cases} 660\left(\frac{1}{20^2} - \xi^2\right)^2 & \text{if} \quad -\frac{1}{20} < \xi < \frac{1}{20}, \\ 0 & \text{otherwise.} \end{cases}$$

The initial velocity for the noisy case is the sum of v_0 from (B2) and a uniformly distributed random variable with mean zero and maximum amplitude 10^{-3}.

B.2 Granular acoustics

The potential is defined as

$$U(\xi) = \begin{cases} C_r\left(\frac{1}{1-p}\xi^{1-p}x_\star - \xi x_\star^{1-p} + \frac{p}{p-1}x_\star^{2-p}\right), & \text{if } \xi \in (0, x_\star] \\ 0, & \text{if } \xi > x_\star \end{cases} \tag{B3}$$

where $p > 1$, $x_\star = L$, and C_r is material stiffness. The potential is plotted in the right panel of Fig. B2 .

The initial velocity in the first example of Subsection 6.2 is given by $v^0 = v^{base} + v^{1,pert}$, where v^{base} is a piecewise cubic continuos function and $v^{1,pert}$ is a Gaussian:

$$v^{base}(q_j^0) = \begin{cases} 0, & \text{if } 0 \le q_j^0 \le L_1, \\ d_1(q_j^0 - x_1)(q_j^0 - L_1)^2, & \text{if } L_1 < q_j^0 \le L_2, \\ d_2, & \text{if } L_2 < q_j^0 \le L_3, \\ d_3(q_j^0 - x_2)(q_j^0 - L_4)^2, & \text{if } L_3 < q_j^0 \le L_4, \\ 0, & \text{if } L_4 < q_j^0 \le L, \end{cases} \qquad j = 1, \dots, N, \tag{B4}$$

$$v^{1,pert}(q_j^0) = a_1 \exp\left(-\frac{(q_j^0 - q^*)^2}{2\sigma^2}\right), \qquad j = 1, \dots, N. \tag{B5}$$

Here $L_1 = 0.2L$, $L_2 = 0.4L$, $L_3 = 0.7L$, $L_4 = 0.9L$, $x_1 = (3L_2 - L_1)/2$, $x_2 = (3L_3 - L_4)/2$, $d_2 = 0.3$, $d_1 = -2d_2/(L_2 - L_1)^3$, $d_3 = -2d_2/(L_3 - L_4)^3$, $a_1 = 0.1$, $q^* = 0.3L$.

The initial velocity in the second example is $v^0 = v^{base} + v^{2,pert}$, where v^{base} is as in (B4) but with $L_1 = 0.1L$, $L_2 = 0.2L$, $L_3 = 0.3L$, $L_4 = 0.6L$ and $v^{2,pert}$ is a sine function on the interval $[0, L_4]$:

$$v^{2,pert}(q_j^0) = \begin{cases} a_2 \sin\left(\frac{2\pi k q_j^0}{L_4}\right), & \text{if} \quad 0 \le q_j^0 \le L_4, \\ 0, & \text{otherwise} \end{cases} \qquad j = 1, \dots, N, \tag{B6}$$

with $a_2 = 5$ and $k = 50$. The sine perturbation has period 0.012.

C FILTERED REGULARIZATION METHODS

In this section, we discuss some filtered regularization methods that can be used to implement deconvolution mentioned in Section 3.3 numerically. Among them are Landweber iteration [30,31], Tikhonov regularization [20] and the truncated SVD method [21].

A *regularization strategy* for solving the integral equation

$$R_\eta[g] = \overline{g}^\eta \tag{C1}$$

where R_η is the convolution operator defined in (3.13), is a family of bounded linear operators Q_η^α parameterized by the *regularization parameter* $\alpha > 0$, and such that

$$Q_\eta^\alpha R_\eta[g] \to g \tag{C2}$$

as $\alpha \to 0$ for all $g \in L^2(\Omega)$ (see e.g. Definition 2.1 in [17]) for a more general definition).

Usually, the right hand side of (C1) is known imprecisely. In the present case the right hand side error represents the difference between the exact averages in (2.6) and (2.7) and their integral approximations (3.1) and (3.2). Let δ be an upper bound on the

norm of this error. A regularization strategy in this case consists of choosing $\alpha(\delta)$. Such a strategy is *admissible* if, as $\delta \to 0$,

$$\alpha(\delta) \to 0 \quad \text{and} \quad \sup\{||Q_\eta^{\alpha(\delta)}[\overline{g}^{\eta,\delta}] - g|| \,:\, ||R_\eta[g] - \overline{g}^{\eta,\delta}|| \le \delta\} \to 0. \tag{C3}$$

Examples of admissible regularization strategies are classical Landweber iteration and Tikhonov regularization. These methods are special cases of the so-called filtered regularization methods and can be related to the singular value decomposition (SVD) of the convolution operator R_η. Another example of the filtered methods is the truncated SVD method. Any filtered method is admissible provided $\alpha(\delta) \to 0$ and $\delta\alpha(\delta) \to 0$ as $\delta \to 0$[17] Thm 2.6.

The Landweber method has recently attracted attention as a means to achieve sub-filter scale resolution in large eddy simulation of turbulence[35],[36]. In the simplest version of the method, approximations g_n to the solution of (C1) are generated by the formula

$$g_n = \sum_{k=0}^{n} (I - R_\eta)^k \overline{g}^\eta, \quad g_0 = \overline{g}^\eta. \tag{C4}$$

The reciprocal of the number n of iterations plays the role of a regularization parameter α. In (C4), I denotes the identity operator.

Tikhonov regularization consists of replacing (C1) by the approximate equation

$$R_\eta[g_\alpha] + \alpha C[g_\alpha] = \overline{g}^\eta. \tag{C5}$$

Here $\alpha > 0$ is a regularization parameter, and C is a stabilizing operator. In practice, C can be an identity, or a suitable differential operator such as Laplacian.

Many regularization methods (Tikhonov, Landweber, truncated SVD) can be conveniently written in terms of SVD and spectral filter functions (see e.g.[17]). This is useful for both discrete and continuous ill-posed problems[21].

The discrete version of the integral equation (C1) is a linear system

$$A\boldsymbol{g} = \overline{\boldsymbol{g}}, \tag{C6}$$

where A is a matrix obtained by the discretization of the integral in the left hand side of (C1), $\boldsymbol{g}$ is a solution, a discrete microscale quantity to be reconstructed, and $\overline{\boldsymbol{g}}$ is the discretization of the corresponding average. To achieve computational efficiency, it is natural to resolve the average $\overline{\boldsymbol{g}}$ (a mesoscale quantity) on a coarse mesh with the size tied to the mesoscale. The solution $\boldsymbol{g}$ (a microscopic quantity) could be rendered on the fine mesh with size εL. This choice of meshes seems to be the most natural for balancing cost and accuracy.

Other mesh combinations can be chosen as well. The least expensive option is to coarsen the discretization of $\boldsymbol{g}$ and solve (C6) entirely on a coarse mesh. In that case, the matrix A is square, and its dimension is determined by the chosen number of the coarse mesh points. The operation count of deconvolution becomes independent of N, but the error in this case appears to be large. Numerical experiments produced significant artifacts, so that the mesoscale details of $\boldsymbol{g}$ could not be reliably reconstructed.

Another possibility is to use a fine mesh for both $\boldsymbol{g}$ and $\overline{\boldsymbol{g}}$. In that case the average would have to be interpolated from the coarse to the fine mesh. The computational cost of deconvolution scales as $O(N^2)$, but this dos not necessarily improve the reconstruction quality, since using a finer discretization increases the condition number of A due to ill-conditioning of the problem.

Ultimately, we chose a more natural two-mesh discretization, whereby $\boldsymbol{g}$ is an N-vector, $\overline{\boldsymbol{g}}$ is a D-vector, with $B < D \ll N$. Recall that B is the number of the mesh nodes associated with the mesh size ηL. Choosing a finer coarse mesh with D nodes enabled us to better resolve the details of size smaller than ηL. Such details may be completely smeared by averaging. In that sense, the length scale associated with D can be called a *sub-filter scale*.

Working with two different meshes, as opposed to using the same mesh, introduces several difficulties. The matrix A in that case is rectangular, and the system (C6) is under-determined. Therefore, (C6) has infinitely many solutions, even when the original integral equation (C1) is uniquely solvable. The general solution is a sum of the particular solution $\boldsymbol{g}^+$ orthogonal to the null space of A and an arbitrary vector from the null space. In the absence of a priori information on the structure of the null space, it is natural to use $\boldsymbol{g}^+$. Thus we set

$$\boldsymbol{g}^+ = A^T \boldsymbol{z},$$

where $\boldsymbol{z}$ is a D-vector to be determined. Assuming that A has full rank and AA^T is invertible (invertibility depends only on the choice of the window function ψ and can be verified prior to running any dynamic simulations), we can set $\boldsymbol{z} = (AA^T)^{-1}\overline{\boldsymbol{g}}$, and

$$\boldsymbol{g}^+ = A^T(AA^T)^{-1}\overline{\boldsymbol{g}}. \tag{C7}$$

It is easy to check that $\boldsymbol{g}^+$ is orthogonal to the null space of A. In (C7), $(AA^T)^{-1}$ denotes either the exact inverse, or a suitable regularized approximation. Typically, singular vectors associated with smaller singular values of A oscillate with higher frequency than the vectors associated with larger singular values. If this holds, then the solution component along the null-space of A is highly oscillatory, while the component orthogonal to the null space is relatively smooth. Therefore, by using $\boldsymbol{g}^+$ and not some other solution, we incorporate additional filtering. This can be useful for taming noise.

Suppose that $\text{rank}(A) = D$. Let $\sigma_j, j = 1, \dots, D$ denote the non-zero singular values of A, and $\boldsymbol{\xi}_j \in \mathbf{R}^D$, $\widehat{\boldsymbol{\xi}}_j \in \mathbf{R}^N$ be the corresponding singular vectors. By the standard properties of SVD,

$$A\widehat{\boldsymbol{\xi}}_j = \sigma_j \boldsymbol{\xi}_j, \qquad A^T \boldsymbol{\xi}_j = \sigma_j \widehat{\boldsymbol{\xi}}_j. \tag{C8}$$

Because the continuum problem (C1) is ill-posed, the singular values are spaced without gaps, and the condition number of A is large. Recall that condition number can be expressed as the ratio of the largest and smallest singular values. In our case, the largest singular value of A is close to one. Therefore, the condition number is approximately equal to the reciprocal of the smallest singular value. The choice of the solution method depends on the condition number and the relative level of noise in $\overline{\boldsymbol{g}}$ and A. The guiding principle it to produce an approximation that would be as close as possible to (C7), without incurring instability. Discretization itself is a mild form of regularization of the original integral equation. Indeed, in the discretized problem, the smallest non-zero singular value is a finite distance away from zero, while in the continuum case zero is an accumulation point of the spectrum. Consequently, if the error in $\overline{\boldsymbol{g}}$ and the condition number of A are small enough, one can use (C7) with no additional regularization. In our case, the integral approximations of the averages are exact when the interpolants are suitably chosen. The only numerical error in the right hand side is the round-off error. Therefore, exact inversion will work when the condition number of A is much smaller than the reciprocal of the machine precision. In practice this means that condition numbers smaller than about 10^8 can be safely handled in this way. For larger condition numbers, exact inversion in (C7) may have to be replaced by a suitable regularized approximation. In this work we use the truncated SVD method. The details are presented next.

The SVD-based implementation of the exact solution is provided by formula (C7). Write

$$\overline{\boldsymbol{g}} = \sum_{j=1}^{D} g_j \boldsymbol{\xi}_j, \qquad \boldsymbol{g}^+ = A^T \left(\sum_{j=1}^{D} z_j \boldsymbol{\xi}_j \right) = \sum_{j=1}^{D} \sigma_j z_j \widehat{\boldsymbol{\xi}}_j, \tag{C9}$$

where the coefficients z_j have to be determined. To obtain the last equality, (C8) was used. Substituting (C9) into (C6) and using orthogonality of $\boldsymbol{\xi}_j$ we deduce

$$z_j = \frac{g_j}{\sigma_j^2}, \tag{C10}$$

which represents (C7) in the basis consisting of singular vectors.

As was explained earlier, formula (C10) may be used when condition number of A is much smaller than the reciprocal of the noise level in the right hand side. Therefore, (C10) becomes unstable when the SVD contains singular values comparable to the machine precision. In that case, as an additional regularization we use the truncated SVD[21]. In this method, the components corresponding to the smallest singular values are discarded. The regularized solution is computed by the formula

$$\boldsymbol{g}^+_{(r)} = \sum_{j=1}^{D} \frac{\phi(\sigma_j)}{\sigma_j} g_j \widehat{\boldsymbol{\xi}}_j, \tag{C11}$$

where the filter function ϕ is defined by

$$\phi(\sigma_j) = \begin{cases} 1 \text{ if } \sigma_j \geq \sigma^* \\ 0 \text{ if } \sigma_j < \sigma^*. \end{cases} \tag{C12}$$

In the above equation σ^* is a cut-off value chosen close to the machine precision. We set $\sigma^* = 10^{-13}$.

It should be noted that since both R_η and A are independent of the microscopic dynamics, the SVD can be pre-computed and used for different right hand sides $\overline{\boldsymbol{g}}$ once the resolution parameters N and D have been fixed. This will decrease the overall computational cost associated with computing the evolution of averages $\overline{\rho}^\eta$, $\overline{\boldsymbol{v}}^\eta$ given by (2.9), (2.10) where stresses are approximated using the regularized deconvolution.

References

1. Kunin I. A.. *Elastic media with microstructure* Series in solids state sciences, vol. 26: . New York: Springer; 1982 /1983.

2. Zhen Y., Vainchtein A.. Dynamics of steps along a martensitic phase boundary. I: Semi-Analytical solution. *J. Mech. Phys. Solids.* 2008;56(2):496–520.

3. Zhen Y., Vainchtein A.. Dynamics of steps along a martensitic phase boundary. II: Numerical simulations. *J. Mech. Phys. Solids.* 2008;56(2):496–520.

4. Truskinovsky L., Vainchtein A.. Kinetics of martensitic phase transitions: Lattice model. *SIAM J. Appl. Math.*. 2005;66(2):533–553.

5. Irving J. H., Kirkwood J. G.. The statistical theory of transport processes IV. The equations of hydrodynamics. *J. Chem. Phys.*. 1950;18:817–829.

6. Noll W.. Der Herleitung der Grundgleichungen der Thermomechanik der Kontinua aus der statistischen Mechanik. *J. Ration. Mech. Anal.*. 1955;4:627–646.

7. Hardy R. J.. Formulas for determining local properties in molecular-dynamics simulations: shock waves. *J. Chem. Phys.*. 1982;76:622–628.

8. Murdoch A. I., Bedeaux D.. Continuum equations of balance via weighted averages of microscopic quantities. *Proc. Royal Soc. London A*. 1994;445:157–179.

9. Murdoch A. I., Bedeaux D.. A microscopic perspective on the physical foundations of continuum mechanics – Part I: macroscopic states, reproducibility, and macroscopic statistics, at prescribed scales of length and time. *Int. J. Engng Sci.*. 1996;34(10):1111–1129.

10. Murdoch A. I., Bedeaux D.. A microscopic perspective on the physical foundations of continuum mechanics – Part II: a projection operator approach to the separation of reversible and irreversible contributions to macroscopic behaviour. *Int. J. Engng Sci.*. 1997;35(10/11):921–949.

11. Murdoch A. I.. A Critique of Atomistic Definitions of the Stress Tensor. *J. Elasticity.* 2007;88:113–140.

12. Seguin B., Fried E.. Statistical foundation of liquid crystal theory: I. Discrete systems of rod-like molecules. *Arch. Rat. Mech. Anal.*. 2012;206(3):1039–1072.

13. Seguin B., Fried E.. Statistical foundation of liquid crystal theory: II. Macroscopic balance laws. *Arch. Rat. Mech. Anal.*. 2013;207(1):1–37.

14. Admal Nikhil Chandra, Tadmor E. B.. A Unified Interpretation of Stress in Molecular Systems. *J. Elast.*. 2010;100(1–2, SI):63–143.

15. Goddard J.. On material velocities and non-locality in the thermo-mechanics of continua. *Int. J. Eng. Sci.*. 2010;48:1279–1288.

16. Groetsch C. W.. *The Theory of Tikhonov Regularization for Fredholm Equation of the First Kind*. Boston: Pitman; 1984.

17. Kirsch A.. *An Introduction to the Mathematical Theory of Inverse Problems*. New York: Springer; 1996.

18. Engl H. W., Hanke M., Neubauer A.. *Regularization of Inverse Problems*. Dordrecht: Kluwer Academic; 1996.

19. Morozov V. A.. *Methods for Solving Incorrectly Posed Problems*. New York: Springer; 1984.

20. Tikhonov A. N., Arsenin V. Y.. *Solutions of Ill-Posed Problems*. New York: Wiley; 1987.

21. Hansen P. Ch.. *Rank-Deficient and Discrete Ill-Posed Problems: Numerical Aspects of Linear Inversion*. SIAM; 1987.

22. Silling S., Lehoucq R. B.. Peridynamic Theory of Solid Mechanics. *Advances in Applied Mechanics.* 2010;44:73–168.

23. Lehoucq R. B., Sears M. P.. The statistical mechanical foundation of the peridynamic nonlocal continuum theory: energy and momentum conservation laws. *Phys. Rev. E.* 2011;84:031112.

24. Coslovich D., Roland C. M.. Heterogeneous slow dynamics and the interaction potential of glass-forming liquids. *J. Non-Crystalline Solids.* 2011;357:397–400.

25. Middleton T. F., Hernandez-Rojas J., Mortenson P. N., Wales D. J.. Crystals of binary Lennard-Jones solids. *Phys. Rev. B.* 2001;64:184201.

26. Mori H., Okamoto H., Isa S.. A simplified theory of liquid-solid transition I. *Prog. Theor. Phys.*. 1972;47(4):1087–1109.

27. Valle R. G. Della, Venuti E.. Quasiharmonic lattice dynamics and molecule dynamics calculations for the Lennard-Jones solids. *Phys Rev. B.* 1998;58(1):206–212.

28. Panchenko A., Barannyk L. L., Gilbert R. P.. Closure method for spatially averaged dynamics of particle chains. *Non-linear Analysis: Real World Applications.* 2011;12:1681–1697.

29. Tartakovsky A., Panchenko A., Ferris K.. Dimension reduction method for ODE fluid models. *J. Comp. Phys.*. 2011;230(23):8554-8572.

30. Fridman V.. A method of successive approximations for Fredholm integral equations of the first kind. *Uspekhi Mat. Nauk*. 1956;11:233–234 (in Russian).

31. Landweber L.. An iteration formula for Fredholm integral equations of the first kind. *Am. J. Math.*. 1951;73:615–624.

32. Tadmor E. B., Miller R. E.. The quasicontinuum method: Overview, applications and current directions.. *J. Comp.-Aided Mater. Design.* 2002;9:203–239.

33. Tadmor E. B., Miller R. E.. *Modeling Materials: Continuum, Atomistic and Multiscale Techniques*. New York: Cambridge University Press; 2012.

34. Barannyk L. L., Panchenko A.. Optimizing performance of the deconvolution model reduction for large ODE systems. *IMA J. Appl. Math.*. to appear;: .

35. Adams N. A., Stolz S.. A subgrid-scale deconvolution approach for shock capturing. *J. Comp. Phys.*. 2002;178(2):391–426.

36. Berselli L. C., Iliescu T., Layton W. J.. *Mathematics of Large Eddy Simulation of Turbulent Flows*. New York: Springer; 2006.

37. Layton W., Lewandowski O.. Residual stress of approximate deconvolution models of turbulence. *J. Turbulence.* 2006;7(46):1–21.

38. Layton W.. Bounds on helicity and dissipation rates of approximate deconvolution models of turbulence. *SIAM J. Math. Anal.*. 2007;39(3):916–931.